

# Guided Formation of 3D Helical Mesostructures by Mechanical Buckling: Analytical Modeling and Experimental Validation

Yuan Liu, Zheng Yan, Qing Lin, Xuelin Guo, Mengdi Han, Kewang Nan, Keh-Chih Hwang, Yonggang Huang, Yihui Zhang,\* and John A. Rogers\*

3D helical mesostructures are attractive for applications in a broad range of microsystem technologies due to their mechanical and electromagnetic properties as stretchable interconnects, radio frequency antennas, and others. Controlled compressive buckling of 2D serpentine-shaped ribbons provides a strategy to formation of such structures in wide ranging classes of materials (from soft polymers to brittle inorganic semiconductors) and length scales (from nanometer to centimeter), with an ability for automated, parallel assembly over large areas. The underlying relations between the helical configurations and fabrication parameters require a relevant theory as the basis of design for practical applications. Here, an analytic model of compressive buckling in serpentine microstructures is presented based on the minimization of total strain energy that results from various forms of spatially dependent deformations. Experiments at micro- and millimeter scales, together with finite element analyses, have been exploited to examine the validity of developed model. The theoretical analyses shed light on general scaling laws in terms of three groups of fabrication parameters (related to loading, material, and 2D geometry), including a negligible effect of material parameters and a square root dependence of primary displacements on the compressive strain. Furthermore, analytic solutions were obtained for the key physical quantities (e.g., displacement, curvature and maximum strain). A demonstrative example illustrates how to leverage the analytic solutions in choosing the various design parameters, such that brittle fracture or plastic yield can be avoided in the assembly process.

## 1. Introduction

3D helical mesostructures hold great potential for a broad range of applications in microsystem technologies, such as microelectromechanical systems (MEMS),<sup>[1,2]</sup> electrodes for lab-on-a-chip systems,<sup>[3,4]</sup> and stretchable electronics.<sup>[5,6]</sup> To form 3D architectures of helical and other relevant topologies at the micro/nanoscale, several classes of fabrication/assembly approaches have been developed by exploiting different working mechanisms.<sup>[2,6–35]</sup> Representative approaches include microcontact printing,<sup>[15,16]</sup> MEMS lithography/electroplating techniques,<sup>[17–19]</sup> manual winding,<sup>[20]</sup> residual-stress-induced self-rolling of thin films/belts,<sup>[21–24]</sup> controlled mechanical buckling,<sup>[6,32]</sup> and 3D additive printing based on direct ink deposition,<sup>[2,25–29]</sup> or direct laser writing<sup>[30,31]</sup> (sometimes in combination with liquid metal paste filling<sup>[29]</sup> or the electrochemical deposition and plasma etching).<sup>[31]</sup> Most of these approaches, such as lithography/electroplating techniques,<sup>[17–19]</sup> manual winding,<sup>[20]</sup> and 3D additive printing,<sup>[2,25–31]</sup> apply directly only to certain classes of materials, e.g., metals

Y. Liu, Prof. K.-C. Hwang, Prof. Y. Zhang  
Center for Mechanics and Materials  
AML

Department of Engineering Mechanics  
Tsinghua University  
Beijing 100084, P. R. China  
E-mail: yihuizhang@tsinghua.edu.cn

Dr. Z. Yan, Q. Lin, X. Guo, K. Nan  
Department of Materials Science and Engineering  
Frederick Seitz Materials Research Laboratory  
University of Illinois at Urbana-Champaign  
Urbana, IL 61801, USA

M. Han  
National Key Laboratory of Science and Technology  
on Micro/Nano Fabrication  
Peking University  
Beijing 100871, P. R. China

Prof. Y. Huang  
Departments of Civil and Environmental Engineering  
and Mechanical Engineering  
Center for Engineering and Health  
Skin Disease Research Center  
Northwestern University  
Evanston, IL 60208, USA

Prof. J. A. Rogers  
Departments of Materials Science and Engineering  
Chemistry, Mechanical Science and Engineering  
Electrical and Computer Engineering  
Beckman Institute for Advanced Science and Technology  
Frederick Seitz Materials Research Laboratory  
University of Illinois at Urbana-Champaign  
Urbana, IL 61801, USA  
E-mail: jrogers@illinois.edu



DOI: 10.1002/adfm.201505132

and/or polymers, and generally not to high-performance semiconductors (e.g., single-crystal silicon) or other advanced materials that are widely adopted in modern high-quality electronics and optoelectronics. Although the methods based on residual-stress-induced self-rolling<sup>[21–24]</sup> are naturally compatible with modern planar technologies and offer yields and throughputs necessary for practical applications, they provide direct access only to certain classes of hollow polyhedral or cylindrical geometries, with the upper length scales limited, to a certain extent, by the achievable levels of residual stresses. In comparison, approaches that rely on buckling in thin 2D ribbons/membranes<sup>[6,14]</sup> allow routes to a broad range of 3D topologies, while offering a natural compatibility with essentially all modern planar technologies, thereby suggesting many possibilities in building sophisticated classes of 3D electronic, optical, and electromagnetic devices. A powerful feature of this approach<sup>[6,14]</sup> is the versatility in the applicable materials, ranging from soft polymers, to brittle inorganic semiconductors, to plastic metals, and length scales, ranging from nanometer, to micrometer, to centimeter dimensions. Recent work includes demonstrations of silicon and/or metallic helical mesostructures in various topologies, including straight helices with different chiralities, double helices, nested helices, toroids, and conical spirals<sup>[6]</sup> by using variants of filamentary serpentine microstructures as the initial 2D patterns. The underlying relations between the 3D configurations, fracture-induced failure, and fabrication related parameters (e.g., prestrain level, the geometric parameters of the serpentine microstructures) require a relevant theory as the basis for the design of structures for specific applications. The mechanics of buckling and postbuckling that govern the 2D–3D transformation are, however, complex, since the deformation of the ribbon-type structures involves not only planar bending, but also twisting and general spatial bending type motions. Previous theories developed either for postbuckling of straight ribbons<sup>[36–40]</sup> or critical buckling of curvy ribbons<sup>[41,42]</sup> cannot be used in the analyses of postbuckling for serpentine microstructures. This paper introduces an analytic model of compressive buckling that is capable of predicting not only the full 3D geometry of helical mesostructures

but also the strain level of relevance to structural reliability. Systematic finite element analyses (FEA) and experimental measurement on 3D helical mesostructures with different geometries validate the utility of the model. The results provide theoretical insight into the scaling laws of deformation and strain with various parameters, including a negligible effect of material parameters and a square root dependence of curvature on the compressive strain. Furthermore, analytic solutions were obtained for the key physical quantities, including the displacement, twist angle, curvature, and strain, which can facilitate design optimization in practical applications.

## 2. An Analytic Model for the Compressive Buckling of Serpentine Microstructures

Figure 1a presents a schematic illustration of the process for forming three chains of helices with different geometries guided by compressive buckling. The initial 2D precursors correspond to thin serpentine microstructures (as shown in the left, bottom panel of Figure 1b) that are strongly bonded, at certain locations (black circles), with a prestrained elastomeric substrate. Releasing the prestrain imparts compressive forces on the serpentine microstructures, thereby lifting the non-bonded locations out of the plane and into 3D configurations. A theoretical model is introduced below to analyze such post-buckling processes, and to determine the full 3D configuration as well as the strain distribution for different initial geometries and prestrain levels.

### 2.1. Geometry, Displacement, and Curvature

Due to the structural periodicity, we focus on the analysis of a representative unit cell in the serpentine microstructure, which consists of two identical arcs, each with a radius of  $R$  and top angle of  $\theta_0$ , as shown in Figure 1b (top). The top angle must be smaller than  $5\pi/3$  to avoid self-overlap of the microstructures, and in practical applications, this parameter is typically in the

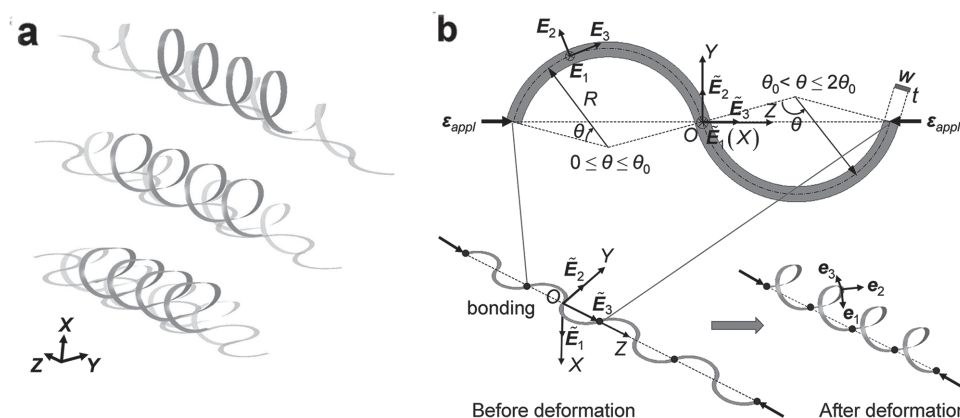


**Figure 1.** Illustration of the buckling-guided formation of 3D helical mesostructures and key dimensions associated with the mechanics model. a) Schematic illustration of the compressive buckling process for 2D serpentine microstructures with three different geometries; b) illustration of the mechanics model and coordinate system, showing the undeformed and deformed configurations. The black dots denote the sites of strong bonding with an elastomeric substrate used in fabrication. A representative unit cell of the serpentine microstructures consists of two identical arcs, each with the radius of  $R$  and top angle of  $\theta_0$ .

range of  $[0, 5\pi/4]$ . To facilitate buckling, the serpentine microstructure usually adopts an ultrathin geometry in which the thickness ( $t$ ) is much smaller than the width ( $w$ ), corresponding to a large cross-sectional aspect ratio (e.g.,  $w/t > 20$ ). This class of serpentine microstructure has been widely explored in various stretchable bioelectronic devices as a key design strategy to achieve system-level stretchability.<sup>[43–52]</sup>

A Cartesian coordinate system ( $X, Y, Z$ ) has its origin at the joint of two arcs, where the  $X$  and  $Z$  axes correspond to the out-of-plane and axial direction of the serpentine microstructure. The unit vectors in such coordinates ( $X, Y, Z$ ) before deformation are  $\tilde{\mathbf{E}}_i (i = 1, 2, 3)$ . A parametric coordinate  $\theta$  (corresponding to the arc length  $S = R\theta$ ) denotes the location along the central axis of the arcs, such that  $\theta \in [0, \theta_0]$  and  $[\theta_0, 2\theta_0]$  represent the first and second arcs, respectively. The initial configuration of the central axis,  $\mathbf{r}_0(\theta) = X_0(\theta)\tilde{\mathbf{E}}_1 + Y_0(\theta)\tilde{\mathbf{E}}_2 + Z_0(\theta)\tilde{\mathbf{E}}_3$ , can be represented by the following parametric equations,

$$\begin{cases} X_0 = 0 \\ Y_0 = R \left[ \cos\left(\frac{\theta_0}{2} - \theta\right) - \cos\frac{\theta_0}{2} \right], \theta \in [0, \theta_0], \text{ and} \\ Z_0 = -R \left[ \sin\frac{\theta_0}{2} + \sin\left(\frac{\theta_0}{2} - \theta\right) \right] \end{cases} \quad (1a)$$

$$\begin{cases} X_0 = 0 \\ Y_0 = -R \left[ \cos\left(-\frac{3\theta_0}{2} + \theta\right) - \cos\frac{\theta_0}{2} \right], \theta \in [\theta_0, 2\theta_0]. \\ Z_0 = R \left[ \sin\frac{\theta_0}{2} + \sin\left(-\frac{3\theta_0}{2} + \theta\right) \right] \end{cases} \quad (1b)$$

In deformation analyses of curvy ribbons, a local coordinate system is usually required to characterize the location of central axis, as illustrated in Figure 1b (top). Before deformation, the corresponding unit vectors are denoted by  $\mathbf{E}_i (i = 1, 2, 3)$ , where  $\mathbf{E}_3$  is the tangential direction;  $\mathbf{E}_1$  and  $\mathbf{E}_2$  lie in the cross-sectional plane, with  $\mathbf{E}_1$  (or equivalently  $\tilde{\mathbf{E}}_1$ ) along the out-of-plane direction and  $\mathbf{E}_2$  the radial direction of the arcs. During the postbuckling, out-of-plane deformations are induced, thereby transforming the central axis into a spatial curve. A material point of this central axis denoted by  $\mathbf{r}_0$  before deformation moves to  $\mathbf{r} = \mathbf{r}_0 + \mathbf{U} = X\tilde{\mathbf{E}}_1 + Y\tilde{\mathbf{E}}_2 + Z\tilde{\mathbf{E}}_3$  after deformation, where  $\mathbf{U}$  is the displacement. The unit vector along the tangential direction of deformed central axis is  $\mathbf{e}_3 = d\mathbf{r}/ds$ , as shown in the right, bottom panel of Figure 1b, where  $s$  denotes the arc length after deformation. The other two unit vectors,  $\mathbf{e}_1$  and  $\mathbf{e}_2$ , involve twisting of the cross section along the central axis, and remain in the cross-sectional plane according to Kirchhoff assumptions. Their derivatives are related to the curvature vector  $\boldsymbol{\kappa}$  by Love<sup>[53]</sup>

$$\frac{\mathbf{e}'_i}{\lambda} = \boldsymbol{\kappa} \times \mathbf{e}_i, \quad (i = 1, 2, 3), \quad (2)$$

where  $(\cdot)' = d(\cdot)/dS$ ;  $\lambda = ds/dS$  is the stretch along the central axis;  $\kappa_1$  and  $\kappa_2$  denote the curvatures in the  $(\mathbf{e}_2, \mathbf{e}_3)$  and  $(\mathbf{e}_1, \mathbf{e}_3)$  surfaces; and the twisting curvature  $\kappa_3$  is related to

the twist angle  $\phi$  of the cross section by  $\kappa_3 = \phi'/\lambda$ . The unit vectors before and after deformation are related by the direction cosine ( $a_{ij}$ , see the Supporting Information for details):

$$\mathbf{e}_i = a_{ij}\mathbf{E}_j, \quad (i = 1, 2, 3, \text{ summation over } j) \quad (3)$$

According to the finite-deformation beam theory,<sup>[39]</sup> the displacement  $\mathbf{U}$  of the central axis and the twist angle  $\phi$  of the cross section can fully characterize the deformation of a curvy beam. For the serpentine microstructure shown in Figure 1b (top), only the left arc is studied in the following, considering its antisymmetric geometry in both the undeformed and deformed configurations. Release of prestrain ( $\epsilon_{\text{pre}}$ ) in an elastomeric substrate induces a compressive strain,  $\epsilon_{\text{appl}} = \epsilon_{\text{pre}}/(1 + \epsilon_{\text{pre}})$ , to the serpentine microstructure, leading to its buckling. During the postbuckling, the displacement ( $\tilde{U}_2$ ) of serpentine microstructures along the  $Y$  axis is negligible,<sup>[6]</sup> since the compression is applied along the  $Z$  axis and the buckling mainly induces out-of-plane displacements (along the  $X$  axis). This characteristic indicates the displacement vector can be simplified as  $\mathbf{U} = \tilde{U}_1\tilde{\mathbf{E}}_1 + \tilde{U}_3\tilde{\mathbf{E}}_3 = U_1\mathbf{E}_1 + U_2\mathbf{E}_2 + U_3\mathbf{E}_3$ , in which  $\tilde{U}_1 = U_1$ . During postbuckling, equilibrium requires that the out-of-plane displacement  $U_1$  and twist angle  $\phi$  have the same order, while the in-plane displacements  $U_2$  and  $U_3$  have the same order as the square of  $U_1$  (or  $\phi$ ),<sup>[39]</sup> i.e.,  $\phi \sim U_1$  and  $U_2 \sim U_3 \sim (U_1)^2$ . Since the axial displacement ( $\tilde{U}_3$ ) induced by the external compression scales with the applied strain  $\epsilon_{\text{appl}}$ , an approximate scaling between the general displacements ( $U_i$  and  $\phi$ ) and applied strain can be obtained

$$\phi \propto \sqrt{\epsilon_{\text{appl}}}, \quad U_1 \propto \sqrt{\epsilon_{\text{appl}}}, \quad U_2 \propto \epsilon_{\text{appl}}, \quad \text{and} \quad U_3 \propto \epsilon_{\text{appl}} \quad (4)$$

The above relations show remarkable agreement with FEA results (Figure S1, Supporting Information). Consistent with intuitive expectation, an approximate proportional relation between the twist angle ( $\phi$ ) and parametric coordinate ( $\theta$ ) is observed in FEA (Figure S2a, Supporting Information), indicating that the twist angle can be given by  $\phi = a\theta\sqrt{\epsilon_{\text{appl}}}$ , with the parameter  $a$  to be determined. FEA results (Figure S2b, Supporting Information) show that the normalized displacement [ $U_1(\theta)/U_1(\theta_0)$ ] is approximately a single-variable function of  $\theta/\theta_0$ , and the distribution of  $U_1$  can be well characterized by (see the Supporting Information for details)

$$U_1 = bR \sin\left(\frac{\pi\theta}{2\theta_0}\right) \left(2 - \frac{\theta}{\theta_0}\right) \left(\frac{\theta}{\theta_0}\right)^2 \sqrt{\epsilon_{\text{appl}}} \quad (5)$$

where  $b$  is a dimensionless parameter to be determined. It should be noticed that the boundary conditions pose additional considerations on the selection of displacement functions in the energy approach. The axial displacement ( $\tilde{U}_3$ ) is comprised of two parts, a uniform part [ $\tilde{U}_{3\text{uniform}} = -\epsilon_{\text{appl}}Z_0(\theta)$ ] due to the global compression from two ends, and a nonuniform part ( $\tilde{U}_{3\text{nonuniform}}$ ) due to local bending and twisting. Since the boundary conditions are expressed directly in terms of the displacement components in the local coordinate system (See Supporting Information for details), the constructions of displacement functions for  $U_{2\text{nonuniform}}$  and  $U_{3\text{nonuniform}}$  are more straightforward. Together with FEA calculations on a wide

range of serpentine geometries (Figure S3, Supporting Information), a set of functions that can both satisfy the boundary conditions and fit well the FEA results are adopted, which read

$$U_{2\text{nonuniform}} = -R\epsilon_{\text{appl}} \cos\left(\frac{\pi\theta}{\theta_0}\right) \left(1 - \frac{\theta}{\theta_0}\right) \left(\frac{\theta}{\theta_0}\right) \times \left[ c_1 \frac{\theta}{\theta_0} \left(2 - \frac{\theta}{\theta_0}\right) + \frac{\theta_0}{2} \sin(\theta_0) \right], \text{ and} \quad (6a)$$

$$U_{3\text{nonuniform}} = R\epsilon_{\text{appl}} \left[ \cos\left(\frac{\theta_0}{2}\right)^2 \cos\left(\frac{\pi\theta}{\theta_0}\right) \left(1 - \frac{\theta}{\theta_0}\right) \theta + c_2 \sin\left(\frac{\pi\theta}{\theta_0}\right) \left(1 - \frac{\theta}{\theta_0}\right)^3 \left(\frac{\theta}{\theta_0}\right) \right] \quad (6b)$$

where  $c_1$  and  $c_2$  are two dimensionless parameters to be determined by the energy minimization detailed in Section 2.2. As shown by Su et al.,<sup>[39]</sup> the work conjugate of the bending moment and torque is  $\hat{\kappa} = \lambda\kappa$ . It can be given in terms of  $U_i$  and  $\phi$  by

$$\hat{\kappa}_1 = -U_2'' + \left(\phi - \frac{U_1}{R}\right) U_1'' - \frac{U_1'^2}{2R} + \frac{U_3'}{R} - \frac{1}{2R} \left(\phi - \frac{U_1}{R}\right)^2 + \frac{1}{R} \quad (7a)$$

$$\hat{\kappa}_2 = U_1'' - \frac{R\phi - U_1}{R^2} \quad (7b)$$

$$\hat{\kappa}_3 = \phi' \quad (7c)$$

where the terms higher than the third power of the displacement components are neglected. Insertion of Equation (5), (6) and  $\phi = a\theta\sqrt{\epsilon_{\text{appl}}}$  into Equation (7) then gives the distribution of curvature components along the 3D helical mesostructures (See Supporting Information for details).

## 2.2. Energy Approach

Due to the ultrathin geometry of the serpentine microstructures, the local strain usually remains at a low level, such that linear elastic constitutive relations can be adopted. As such, the total strain energy ( $\Pi_{\text{tot}}$ ) mainly consists of in-plane bending energy, out-of-plane bending energy, and twisting energy, and can be written as

$$\begin{aligned} \Pi_{\text{tot}} &= EI_1 \int_0^{\theta_0} \left(\hat{\kappa}_1 - \frac{1}{R}\right)^2 dS + EI_2 \int_0^{\theta_0} \hat{\kappa}_2^2 dS + GI_p \int_0^{\theta_0} \hat{\kappa}_3^2 dS \\ &= EI_1 R \left[ \left(\frac{w}{t}\right)^2 \int_0^{\theta_0} \left(\hat{\kappa}_1 - \frac{1}{R}\right)^2 d\theta + \int_0^{\theta_0} \hat{\kappa}_2^2 d\theta + \frac{2}{1+\nu} \int_0^{\theta_0} \hat{\kappa}_3^2 d\theta \right] \end{aligned} \quad (8)$$

for a unit cell of the serpentine microstructure, where  $EI_1 = (Ew^3t)/12$  and  $EI_2 = (Ewt^3)/12$  are the in-plane and out-of-plane bending stiffness, respectively,  $GI_p \approx (Gwt^3)/3$  is the

twisting stiffness for thin ribbons, and  $\nu$  is the Poisson ratio. Since the serpentine microstructures are highly flexible, the membrane energy is neglected in Equation (8), which can be introduced as a constraint during the energy minimization. Such constraint can be written in the following form

$$\int_0^{\theta_0} \left\{ \left[ \frac{dX(\theta)}{d\theta} \right]^2 + \left[ \frac{dY(\theta)}{d\theta} \right]^2 + \left[ \frac{dZ(\theta)}{d\theta} \right]^2 - R^2 \right\} d\theta = 0 \quad (9)$$

For any prescribed geometries ( $w/t$ ,  $w/R$ , and  $\theta_0$ ) and external strain ( $\epsilon_{\text{appl}}$ ), minimization of the total energy by searching over a reasonable range for each dimensionless parameter ( $a$ ,  $b$ ,  $c_1$ , and  $c_2$ ) then gives solutions for the four unknowns. The process can be implemented numerically (e.g., using commercial software MAPLE or MATLAB). After the determination of displacement components ( $\phi$ ,  $U_1$ ,  $U_2$ , and  $U_3$ ), the coordinates of every material point in the serpentine microstructure can be obtained, thereby giving the full 3D helical configuration during postbuckling. Equation (8) indicates that the change of in-plane bending curvature should be much smaller than the counterpart of out-of-plane bending and twisting, for ultrathin (i.e.,  $w/t > 20$ ) geometries of 2D precursors, because of the large coefficient ( $w^2/t^2$ ) in the corresponding energy term.

## 2.3. Validation of the Model by Experiments and FEA

Two different sets of experiments (see the Experimental Section for details) using microscale structures in a photodefinable epoxy (SU8) and millimeter-scale features in plastic, as well as 3D FEA serve to validate the models. Figure 2a and Figure S4 (Supporting Information) present the model predictions, FEA calculations, and experimental results on the deformed configurations under three different levels of applied strain for a wide range of serpentine geometries (with the arc angle from 30° to 210°). The extent of twisting increases evidently with the arc angle increasing from 30° to 210°. Good agreements can be observed for all of the different geometries and loading levels. Figure 2b–d illustrates the distribution of dimensionless displacement components ( $\phi/\theta_0$ ,  $\tilde{U}_1/L$ , and  $\tilde{U}_3/L$ , with  $L = R\theta_0$  denoting the arc length) for a representative 3D helical mesostructure (with  $\theta_0 = 150^\circ$ ) under different levels of applied strain, which provides quantitative evidence on the accuracy of analytic model. Both the out-of-plane displacement ( $\tilde{U}_1/L$ ) and twist angle ( $\phi/\theta_0$ ) reach their maximum magnitudes at the center of 3D helical mesostructures. The distribution of dimensionless in-plane displacements ( $U_2/L$  and  $U_3/L$ ) in the local coordinate system appears in Figure S5 (Supporting Information).

## 3. Results and Discussions

The model can be used to analyze the effects of various geometric and material parameters on the 3D helical mesostructures, aiming to establish useful scaling laws that can facilitate the design optimization in practical applications. In general, the final 3D helical configurations might be affected by three

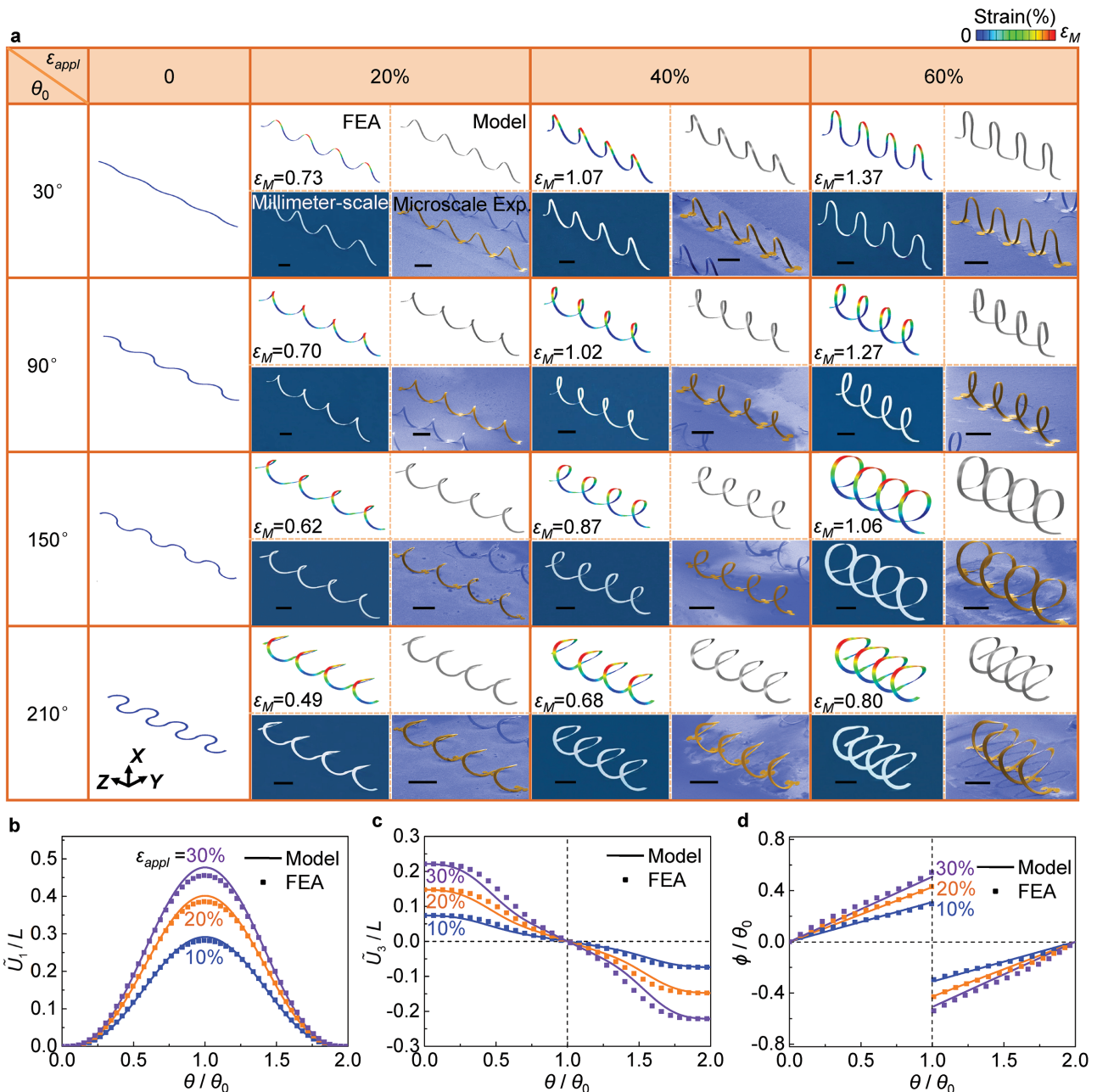


**Figure 2.** Experimental, numerical, and analytical studies of the buckling deformations. a) Modeling, FEA, optical images (millimeter-scale experiment), and colorized scanning electron microscope (SEM) (microscale experiment) images of 3D helical mesostructures with different arc angles (30°, 90°, 150°, and 210°) under different levels of compressive strains (0%, 20%, 40%, and 60%). The color of the FEA results represents the magnitude of maximum principal strain. All of the scale bars in the micro- and millimeterscale experiments are 500  $\mu\text{m}$  and 5 mm, respectively. b–d) Analytic and FEA results on the distribution of dimensionless pop-up displacement, axial displacement, and twist angle for the helical mesostructures (with  $\theta_0 = 150^\circ$ ) under different levels of compressive strains. The geometric parameters include ( $w/R = \theta_0/17$ ,  $t = 75 \mu\text{m}$  and  $w = 900 \mu\text{m}$ ) for modeling, FEA, and millimeter-scale experiment, and [ $w/R = \theta_0/17$ ,  $t = 7 \mu\text{m}$  and  $w \approx 61 \mu\text{m}$  for  $\theta_0 = 30^\circ, 90^\circ$ , and  $150^\circ$  (or  $w \approx 65 \mu\text{m}$  for  $\theta_0 = 210^\circ$ )] for microscale experiment.

groups of fabrication-related parameters: (1) loading parameter ( $\epsilon_{appl}$ ); (2) material parameters ( $E$  and  $\nu$ ); (3) geometric parameters ( $w/t$ ,  $w/R$ , and  $\theta_0$ ). The theoretical analyses in Section 2.1 already reveal the dependence [Equation (4)] of displacement components on the applied strain. Furthermore, the expression [Equation (8)] of total strain energy indicates that the modulus ( $E$ ) has essentially no effect on the minimization process, and

hence, makes no difference on the 3D configurations. While the Poisson ratio ( $\nu$ ) influences the twisting energy in Equation (8), both analytic and FEA results show that this material parameter has negligible effects on the primary displacements ( $\phi/\theta_0$  and  $U_1/L$ ) during postbuckling, as shown in Figure 3a and Figure S6a (Supporting Information), for  $\nu$  varying in a wide range of [0, 0.5]. This feature is also in accordance with

the experiment results in Figure 2a, where two different types of materials (epoxy and plastic) result in nearly the same helical configurations. For thin, slender serpentine microstructures, e.g., with  $w/t > 20$  and  $w/R < 0.3$ , the cross-sectional geometric parameters ( $w/t$  and  $w/R$ ) also play negligible roles on the primary displacements (Figures S6b,c and S7, Supporting Information), in accordance with our intuitive expectations. The relatively large discrepancy between analytic and FEA results for relatively wide serpentine precursors (e.g.,  $w/R \approx 0.4$ ) is attributed to the neglect of transverse shear effect in the current analytic model. Based on the above analyses, it can be deduced that the dimensionless parameters ( $a$ ,  $b$ ,  $c_1$ , and  $c_2$ ) are merely dependent on a single geometric parameter ( $\theta_0$ ) for thin, slender serpentine microstructures. As such, approximate solutions to the parameters ( $a$  and  $b$ ) related to the primary displacements ( $\phi$  and  $U_1$ ) can be obtained by fitting the analytic results for a wide range of arc angle ( $\theta_0$ ) as

$$a(\theta_0) = 1.72 - 0.29\theta_0, \quad b(\theta_0) = (1.23 - 0.14\theta_0)\theta_0 \quad (10)$$

Thereby, approximate solutions of  $\phi$  and  $U_1$  are given by

$$\begin{aligned} \phi &= (1.72 - 0.29\theta_0)\theta\sqrt{\varepsilon_{\text{appl}}}, \\ U_1 &= R\theta_0(1.23 - 0.14\theta_0)\sin\left(\frac{\pi\theta}{2\theta_0}\right)\left(2 - \frac{\theta}{\theta_0}\right)^2\left(\frac{\theta}{\theta_0}\right)^2\sqrt{\varepsilon_{\text{appl}}} \end{aligned} \quad (11)$$

The predictions of Equation (11) agree reasonably well with the precise model calculations (according to energy minimization) and FEA results, as shown in Figure 3b, c and Figure S6d, e (Supporting Information). Taking the limit  $\theta_0 \rightarrow 0$  by fixing  $L = R\theta_0$ , the 2D serpentine precursor degenerates into a straight ribbon, and the resulting out-of-plane displacement ( $U_1/L$ ) and twist angle ( $\phi$ ) approach the counterparts for buckled structures that arise from straight ribbons [Figure 3c and Figure S6e (Supporting Information)].

Since the 3D helical mesostructures studied above are formed from compressive buckling that includes both bending and twisting deformations, a physical quantity, namely, the mode ratio ( $\rho$ ), is introduced as a metric to classify the resulting 3D mesostructures into two different groups, i.e., the bending dominated and bending-twisting mixed modes.<sup>[6]</sup> This quantity is defined by the ratio of the average twisting curvature ( $|\hat{\kappa}_2|_{\text{avg}}$ ) to the average out-of-plane bending curvature ( $|\hat{\kappa}_3|_{\text{avg}}$ ),

recognizing the negligible change of in-plane bending curvature for ultrathin (i.e.,  $w/t > 20$ ) 2D precursors. For the serpentine microstructures used as 2D precursors, the out-of-plane bending and twisting curvatures can be solved by inserting Equation (11) into Equation (7), leading to

$$\hat{\kappa}_2 = \frac{\sqrt{\varepsilon_{\text{appl}}}}{4R\theta_0^3} F_1(\theta, \theta_0) = \frac{\sqrt{\varepsilon_{\text{appl}}}}{4R\theta_0^3} \begin{pmatrix} (1.23 - 0.14\theta_0)[4\theta_0^2(\theta^4 - 4\theta\theta^3 + 4\theta^2\theta^2 + 12\theta^2) \\ -24\theta_0\theta + 8\theta_0^3] - \pi^3\theta^2(\theta - 2\theta_0)^2 \sin\left(\frac{\pi\theta}{2\theta_0}\right) \\ +16\pi(1.23 - 0.14\theta_0)\theta_0\theta(\theta^2 - 3\theta_0\theta + 2\theta_0^2) \cos\left(\frac{\pi\theta}{2\theta_0}\right) \\ -4(1.72 - 0.29\theta_0)\theta_0^2\theta \end{pmatrix} \quad (12a)$$

$$\hat{\kappa}_3 = \frac{(1.72 - 0.29\theta_0)\sqrt{\varepsilon_{\text{appl}}}}{R} \quad (12b)$$

The mode ratio can be obtained accordingly as

$$\rho = \frac{\int_0^{\theta_0/R} |\hat{\kappa}_2| dS}{\int_0^{\theta_0/R} |\hat{\kappa}_3| dS} = \frac{\int_0^{\theta_0} |F_1(\theta, \theta_0)| d\theta}{4(1.72 - 0.29\theta_0)\theta_0^2} \quad (13)$$

which is a single-variable function independent of the applied strain. Equations (12a) and (12b) show that the twisting curvature remains almost unchanged in the helical mesostructures, while the bending curvature varies systematically, reaching its peak at the inner region of the mesostructures. These findings capture the distribution features of both curvature components (Figure S8, Supporting Information). Figure 4 presents the variations of dimensionless average curvatures ( $R|\hat{\kappa}_2|_{\text{avg}}$  and  $R|\hat{\kappa}_3|_{\text{avg}}$ ) and the mode ratio with two key parameters (applied strain  $\varepsilon_{\text{appl}}$  and arc angle  $\theta_0$ ). The results confirm the square root scaling of average curvatures with the applied strain, as well as the strain-independent feature of mode ratio. With increasing the arc angle ( $\theta_0$ ), the twisting curvature decreases almost in a linear manner, while the bending curvature decreases much faster (Figure 4d,e). Both FEA and theoretical results (Figure 4f) indicate a nearly proportional dependence of mode ratio on the arc angle, i.e.,  $\rho \approx 0.41\theta_0$ , in which the coefficient of proportionality is determined from the Taylor expansion of Equation (13).

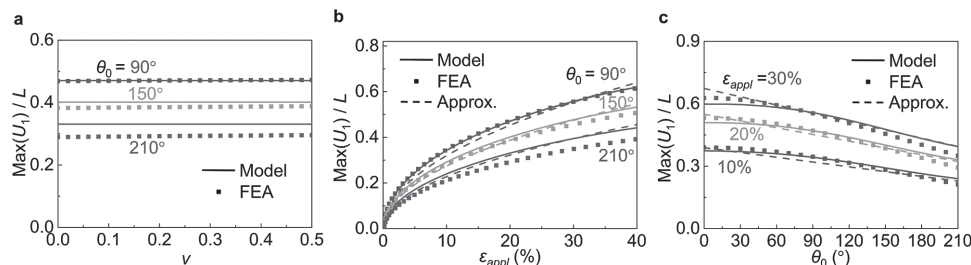


**Figure 3.** Influence of various geometric and material parameters on the out-of-plane displacement. Results of precise model calculation, approximate solution, and FEA for the dimensionless maximum out-of-plane displacement versus a) the Poisson ratio and b) applied strain for helical mesostructures with three different arc angles ( $\theta_0 = 90^\circ$ ,  $150^\circ$ , and  $210^\circ$ ). c) Dimensionless maximum out-of-plane displacement versus the arc angle for helical mesostructures with three different applied strains ( $\varepsilon_{\text{appl}} = 10\%$ ,  $20\%$ , and  $30\%$ ). The parameters adopted in the calculations include  $w/R = 0.05$ ,  $w/t = 50$ , and  $\varepsilon_{\text{appl}} = 20\%$  for (a), and  $w/R = 0.05$ ,  $w/t = 50$ , and  $\nu = 0.27$  for (b) and (c).

Therefore, the use of a large arc angle for the serpentine precursor can enhance the contribution of twisting deformation evidently. Figure S9 (Supporting Information) presents additional results of FEA and model predictions for the curvatures and mode ratio, which illustrate the negligible effects of Poisson ratio, cross-sectional aspect ratio, and normalized width for the geometries of our current interest.

The curvatures decide not only the mode ratio but also the maximum strain in the helical mesostructures, which is directly related to material failure (e.g., brittle fracture for silicon or plastic yield for metals). Specifically, the maximum normal strain  $\varepsilon_{\text{bending}}$  and shear strain  $\gamma_{\text{twisting}}$  of a certain cross section correlate with the curvature components by  $\varepsilon_{\text{bending}} = t|\hat{\kappa}_2|/2$  and  $\gamma_{\text{twisting}} = t|\hat{\kappa}_3|$ . According to FEA and model calculations, the maximum strain typically occurs at the center of the helical mesostructures. Hence, the maximum magnitude of the principal strain in the helical mesostructure can be obtained as

$$\varepsilon_M = F_2(\theta_0) \frac{t}{R} \sqrt{\varepsilon_{\text{appl}}}, \quad (14a)$$

where  $F_2$  is a function given by

$$F_2(\theta_0) = \frac{4a(\theta_0)\theta_0^3 + b(\theta_0)(16 + \pi^2 - 4\theta_0^2) + \sqrt{16a(\theta_0)^2\theta_0^6(1 + \theta_0^2) + b(\theta_0)^2(16 + \pi^2 - 4\theta_0^2)^2 + 8a(\theta_0)b(\theta_0)\theta_0^3(16 + \pi^2 - 4\theta_0^2)}}{16\theta_0^2} \quad (14b)$$

Equation (14) shows that the maximum strain ( $\varepsilon_M$ ) is determined by the applied strain ( $\varepsilon_{\text{appl}}$ ), arc angle ( $\theta_0$ ), and normalized thickness ( $t/R$ ), and is independent of the other parameters (Poisson ratio  $\nu$  and normalized width  $w/R$ ), which is in accordance with FEA results (Figure S10, Supporting Information). Figure 5a–c demonstrates that the predictions

of analytic solution [Equation (14)] exhibit reasonable agreement with the FEA and precise model calculations, with both in support of the proportional scaling of maximum strain with the square root of applied strain and the normalized thickness. Here, the discrepancy between theoretical predictions and FEA can be mainly attributed to the overestimate of the bending curvature (Figure S8, Supporting Information). The increase in the arc angle results in a substantial reduction in the maximum strain, e.g., by  $\approx 0.6$  times from  $\theta_0 = 90^\circ$  to  $180^\circ$ , suggesting an effective route to enhancing the compressibility of the helical mesostructures.

As mentioned previously, the buckling guided fabrication process relies on the release of prestrain in the elastomeric substrate to provide compressive forces to the serpentine precursors. An excessively large prestrain can, thereby, lead to failure in the constituent material. Here, a failure criterion based on the maximum principal strain is adopted for simplicity, in which the threshold ( $\varepsilon_{\text{threshold}}$ ) is assumed to be independent of thickness. Based on Equation (14a), the applied strain–prestrain relation,  $\varepsilon_{\text{appl}} = \varepsilon_{\text{pre}}/(1 + \varepsilon_{\text{pre}})$  and the failure criterion of  $\varepsilon_M = \varepsilon_{\text{threshold}}$ , the maximum prestrain ( $\varepsilon_{\text{pre}}^{\text{max}}$ ) that can be used to avoid material failure is determined as

$$\varepsilon_{\text{pre}}^{\text{max}} = \left[ \frac{R\varepsilon_{\text{threshold}}}{tF_2(\theta_0)} \right]^2 / \left\{ 1 - \left[ \frac{R\varepsilon_{\text{threshold}}}{tF_2(\theta_0)} \right]^2 \right\}, \quad (15)$$

for  $\varepsilon_{\text{threshold}} < \frac{tF_2(\theta_0)}{R}$

When  $\varepsilon_{\text{threshold}} \geq tF_2(\theta_0)/R$ , there is no upper limit for the prestrain, and any level of prestrain would not lead to material failure. In the following analyses, the threshold strain ( $\varepsilon_{\text{threshold}}$ ) is taken as the fracture limit for brittle materials (e.g., 2% for silicon), or the yield strain for metallic materials (e.g., 0.3% for gold). Figure 5d shows the predicted maximum prestrains for silicon and gold helical mesostructures with a

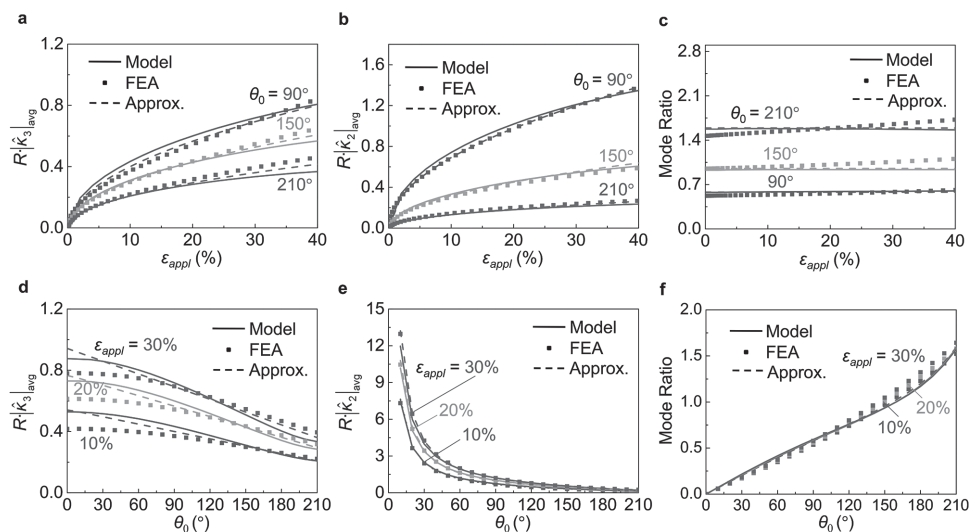


**Figure 4.** Influence of geometric parameters on the curvature and mode ratio. Results of precise model calculation, approximate solution, and FEA a,b) for dimensionless average curvatures and c) mode ratio versus the applied strain for helical mesostructures with three different arc angles ( $\theta_0 = 90^\circ$ ,  $150^\circ$ , and  $210^\circ$ ). d,e) Dimensionless average curvatures and f) mode ratio versus the arc angle for helical mesostructures with three different applied strains ( $\varepsilon_{\text{appl}} = 10\%$ ,  $20\%$ , and  $30\%$ ). The parameters adopted in the calculations include  $w/R = 0.05$ ,  $w/t = 50$ , and  $\nu = 0.27$ .

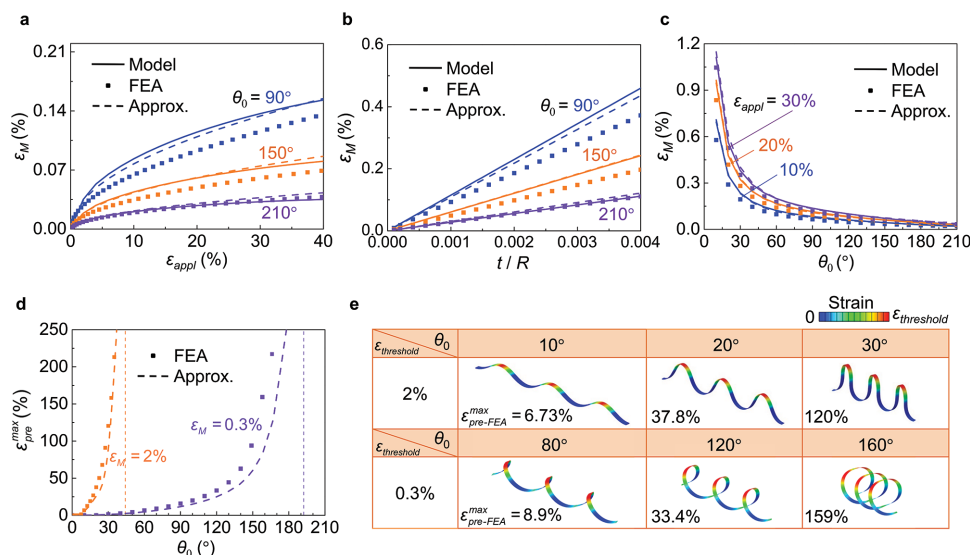


**Figure 5.** Strain analyses for avoiding failure of helical mesostructures during postbuckling. Results of precise model calculation, approximate solution, and FEA for maximum principal strain of material versus a) the applied strain, b) normalized thickness, and c) arc angle. d) Maximum prestrain that can be used in the elastomeric substrate, to avoid brittle fracture in the silicon helical mesostructures (according to  $\epsilon_M = 0.3\%$ ) or to avoid plastic yield in the gold helical mesostructures (according to  $\epsilon_M = 0.3\%$ ). e) Deformed configurations of six different helical mesostructures when the maximum strain reaches the corresponding failure threshold in which the color of FEA results represents the magnitude of maximum principal strain. The parameters adopted in the calculations include  $t/R = 0.001$  for (a), (c), (d), and (e), and  $\epsilon_{\text{appl}} = 20\%$  for (b).

representative normalized thickness ( $t/R = 0.001$ ) and a broad range of arc angles. Both the analytic and FEA results show a higher  $\epsilon_{\text{pre}}^{\text{max}}$  at a larger  $\theta_0$ , and hence, that a more compact helical mesostructures can be achieved (Figure 5e). When the arc angle is sufficiently large, e.g.,  $> 192^\circ$  (corresponding to the vertical dashed line in Figure 5d), such that  $\epsilon_{\text{threshold}} \geq tF_2(\theta_0)/R$  holds true, the gold helical mesostructures are always safe from yield, for any level of prestrain.

Due to the mechanical and electromagnetic properties, the helical mesostructures can be exploited as stretchable interconnects or functional components (e.g., inductors or antennas), which could yield a stretchability higher than the prestrain ( $\epsilon_{\text{pre}}$ ) used in the assembly, in the case when no solid encapsulates the devices. When a helical mesostructure is axially stretched ( $\epsilon_{\text{stretch}} \leq \epsilon_{\text{pre}}$ ), the out-of-plane displacement, the curvature components, as well as the maximum principal strain still follow a similar square root scaling

$$U_1, \hat{\kappa}_2, \hat{\kappa}_3, \epsilon_M \propto \sqrt{\frac{\epsilon_{\text{pre}}}{1 + \epsilon_{\text{pre}}} - \frac{\epsilon_{\text{stretch}}}{1 + \epsilon_{\text{stretch}}}}, \text{ for } \epsilon_{\text{stretch}} \leq \epsilon_{\text{pre}} \quad (16)$$

This scaling agrees well with the FEA results in Figure S11 (Supporting Information).

#### 4. Conclusion

The work presented here represents systematic studies toward buckling-guided formation of 3D helical mesostructures, through combined analytic modeling, FEA, and experiment. The analytic models, validated by FEA and experiment, suggest negligible roles of material parameters ( $E$  and  $\nu$ ) and cross-sectional geometric parameters ( $w/t$  and  $w/R$ ), with dominant

roles of applied strain ( $\epsilon_{\text{appl}}$ ) and arc angle ( $\theta_0$ ), on the final 3D configurations. The resulting scaling laws enable predictions of key physical quantities, including displacement, curvature, mode ratio, and strain, using approximate analytic solutions. A demonstrative example based on analytic solutions illustrates how to select key design parameters (e.g., the prestrain of substrate and geometry of serpentine microstructures), such that brittle fracture or plastic yield can be avoided. Further work could follow by extension of the scaling laws to 2D precursors with membrane configurations. These results can be used as design references for future optimizations in practical applications.

#### 5. Experimental Section

Preparation of 3D helical mesostructures began with thermal oxidation to form a layer of silicon dioxide ( $\text{SiO}_2$ , 500 nm in thickness) on a silicon wafer. Next, spin casting and photolithography formed patterns of photodefinable epoxy (SU8, 7  $\mu\text{m}$  in thickness) on the  $\text{SiO}_2$ . Immersion in hydrofluoric acid (HF) removed the buried  $\text{SiO}_2$  layer from the exposed regions and also slightly from under the edges of the SU8. Spin casting and photolithography created patterns of photoresist (AZ 5214, 4  $\mu\text{m}$  in thickness) on top of the SU8 layers to define the bonding sites. Immersion in HF eliminated the remaining  $\text{SiO}_2$  by complete undercut etching. The techniques of transfer printing enabled retrieval of the 2D precursors and their delivery to a piece of water soluble tape (polyvinyl alcohol, PVA). A thin sheet ( $\approx 0.5$  mm) of silicone elastomer (Dragon Skin, Smooth-On) served as the substrate, stretched to well-defined levels of prestrain using a customized stage. Exposing the prestrained elastomer and the 2D precursors (on PVA) to UV-induced ozone yielded hydroxyl termination on their exposed surfaces. Laminating the tape onto the elastomer substrate with the exposed SU8 side down, followed by baking in an oven at 70  $^\circ\text{C}$  for 10 min yielded strong covalent bonds via condensation reactions of surface-enriched hydroxyl groups between the elastomer substrate

and the exposed regions of 2D precursors. Washing with hot water and then acetone dissolved the PVA tape and the photoresist. Slowly releasing the prestrain completed the process for assembly of 3D helical mesostructures.

Preparation of helical mesostructures in plastic films began with mechanical cutting of a thin layer ( $\approx 75 \mu\text{m}$  in thickness) into desired serpentine patterns, followed by cutting of bonding locations in a thin sheet of paper ( $\approx 90 \mu\text{m}$  in thickness). The pattern of bonding locations corresponds to a certain level of compressive strain applied to the serpentine microstructure. Adhering this paper layer onto a rigid plastic substrate through thin, double-coated tape (9080A, 3M, Minnesota, USA) exposed adhesive bonding locations for purposes of assembly. Adhering the 2D serpentine microstructure at the exposed bonding locations yielded the corresponding 3D helical mesostructures.

## Supporting Information

Supporting Information is available from the Wiley Online Library or from the author.

## Acknowledgements

Y.L. and Z.Y. contributed equally to this work. Y.Z. acknowledges the support from the Thousand Young Talents Program of China and the National Science Foundation of China (Grant No. 11502129). J.A.R. acknowledges the support from the U.S. Department of Energy, Office of Science, Basic Energy Sciences under Award # DE-FG02-07ER46471. Y.H. and J.A.R. acknowledge the support from the NSF (Grant No. CMMI-1400169) and the NIH (Grant No. R01EB019337). K.-C.H. acknowledges the support from the National Basic Research Program of China (Grant No. 2015CB351900).

Received: November 30, 2015

Revised: January 17, 2016

Published online: February 24, 2016

- [1] R. N. Dean, P. C. Nordine, C. G. Christodoulou, *Microw. Opt. Technol. Lett.* **2000**, *24*, 106.
- [2] R. D. Farahani, H. Dalir, V. Le Borgne, L. A. Gautier, M. A. El Khakani, M. Levesque, D. Therriault, *Nanotechnology* **2012**, *23*, 085502.
- [3] Y. B. Huang, L. Y. He, H. Y. Jiang, Y. X. Chen, *Int. J. Mol. Sci.* **2012**, *13*, 6849.
- [4] S. G. He, F. Chen, K. Y. Liu, Q. Yang, H. W. Liu, H. Bian, X. W. Meng, C. Shan, J. H. Si, Y. L. Zhao, X. Hou, *Opt. Lett.* **2012**, *37*, 3825.
- [5] F. Xu, W. Lu, Y. Zhu, *ACS Nano* **2011**, *5*, 672.
- [6] S. Xu, Z. Yan, K.-I. Jang, W. Huang, H. Fu, J. Kim, Z. Wei, M. Flavin, J. McCracken, R. Wang, A. Badea, Y. Liu, D. Xiao, G. Zhou, J. Lee, H. U. Chung, H. Cheng, W. Ren, A. Banks, X. Li, U. Paik, R. G. Nuzzo, Y. Huang, Y. Zhang, J. A. Rogers, *Science* **2015**, *347*, 154.
- [7] T. Castle, Y. G. Cho, X. T. Gong, E. Y. Jung, D. M. Sussman, S. Yang, R. D. Kamien, *Phys. Rev. Lett.* **2014**, *113*, 245502.
- [8] M. Eidini, G. H. Paulino, *Sci. Adv.* **2015**, *1*, e1500224.
- [9] E. T. Filipov, T. Tachi, G. H. Paulino, *Proc. Natl. Acad. Sci. USA* **2015**, *112*, 12321.
- [10] T. G. Leong, A. M. Zarafshar, D. H. Gracias, *Small* **2010**, *6*, 792.
- [11] V. Y. Prinz, D. Grutzmacher, A. Beyer, C. David, B. Ketterer, E. Deckardt, *Nanotechnology* **2001**, *12*, 399.
- [12] O. G. Schmidt, K. Eberl, *Nature* **2001**, *410*, 168.
- [13] D. M. Sussman, Y. Cho, T. Castle, X. T. Gong, E. Jung, S. Yang, R. D. Kamien, *Proc. Natl. Acad. Sci. USA* **2015**, *112*, 7449.
- [14] Y. H. Zhang, Z. Yan, K. W. Nan, D. Q. Xiao, Y. H. Liu, H. W. Luan, H. R. Fu, X. Z. Wang, Q. L. Yang, J. C. Wang, W. Ren, H. Z. Si, F. Liu, L. H. Yang, H. J. Li, J. T. Wang, X. L. Guo, H. Y. Luo, L. Wang, Y. G. Huang, J. A. Rogers, *Proc. Natl. Acad. Sci. USA* **2015**, *112*, 11757.
- [15] R. J. Jackman, J. L. Wilbur, G. M. Whitesides, *Science* **1995**, *269*, 664.
- [16] J. A. Rogers, R. J. Jackman, G. M. Whitesides, *J. Microelectromech. Syst.* **1997**, *6*, 184.
- [17] J. W. Choi, R. B. Wicker, S. H. Cho, C. S. Ha, S. H. Lee, *Rapid Prototyping J.* **2009**, *15*, 59.
- [18] T. Horiuchi, H. Ishii, Y. Shinozaki, T. Ogawa, *Microelectron. Eng.* **2011**, *88*, 2567.
- [19] T. Horiuchi, H. Ishii, Y. Shinozaki, T. Ogawa, K. Kojima, *Jpn. J. Appl. Phys.* **2011**, *50*, 06gm10.
- [20] D. L. Olson, T. L. Peck, A. G. Webb, R. L. Magin, J. V. Sweedler, *Science* **1995**, *270*, 1967.
- [21] S. V. Golod, V. Y. Prinz, V. I. Mashanov, A. K. Gutakovskiy, *Semicond. Sci. Technol.* **2001**, *16*, 181.
- [22] D. J. Bell, T. E. Bauert, L. Zhang, L. X. Dong, Y. Sun, D. Grutzmacher, B. J. Nelson, *Nanotechnology* **2007**, *18*, 055304.
- [23] X. Y. Kong, Z. L. Wang, *Nano Lett.* **2003**, *3*, 1625.
- [24] W. Huang, X. Yu, P. Froeter, R. M. Xu, P. Ferreira, X. L. Li, *Nano Lett.* **2012**, *12*, 6283.
- [25] A. Yamada, F. Niikura, K. Ikuta, *J. Micromech. Microeng.* **2008**, *18*, 025035.
- [26] J. Hu, M. F. Yu, *Science* **2010**, *329*, 313.
- [27] L. L. Lebel, B. Aissa, M. A. El Khakani, D. Therriault, *Adv. Mater.* **2010**, *22*, 592.
- [28] S. Z. Guo, F. Gosselin, N. Guerin, A. M. Lanouette, M. C. Heuzey, D. Therriault, *Small* **2013**, *9*, 4118.
- [29] S. Y. Wu, C. Yang, W. Hsu, L. W. Lin, *Microsyst. Nanoeng.* **2015**, *1*, 15013.
- [30] C. N. LaFratta, L. J. Li, J. T. Fourkas, *Proc. Natl. Acad. Sci. USA* **2006**, *103*, 8589.
- [31] J. K. Gansel, M. Thiel, M. S. Rill, M. Decker, K. Bade, V. Saile, G. von Freymann, S. Linden, M. Wegener, *Science* **2009**, *325*, 1513.
- [32] Y. G. Sun, W. M. Choi, H. Q. Jiang, Y. G. Y. Huang, J. A. Rogers, *Nature Nanotechnol.* **2006**, *1*, 201.
- [33] R. D. Farahani, K. Chizari, D. Therriault, *Nanoscale* **2014**, *6*, 10470.
- [34] Y. Klein, E. Efrati, E. Sharon, *Science* **2007**, *315*, 1116.
- [35] V. B. Shenoy, D. H. Gracias, *MRS Bull.* **2012**, *37*, 847.
- [36] Z. Y. Huang, W. Hong, Z. Suo, *J. Mech. Phys. Solids* **2005**, *53*, 2101.
- [37] H. Q. Jiang, Y. G. Sun, J. A. Rogers, Y. G. Huang, *Appl. Phys. Lett.* **2007**, *90*, 133119.
- [38] H. Q. Jiang, Y. G. Sun, J. A. Rogers, Y. G. Huang, *Int. J. Solids Struct.* **2008**, *45*, 2014.
- [39] Y. W. Su, J. Wu, Z. C. Fan, K. C. Hwang, J. Z. Song, Y. G. Huang, J. A. Rogers, *J. Mech. Phys. Solids* **2012**, *60*, 487.
- [40] J. Song, H. Jiang, W. M. Choi, D. Y. Khang, Y. Huang, J. A. Rogers, *J. Appl. Phys.* **2008**, *103*, 014303.
- [41] L. Giomi, L. Mahadevan, *Phys. Rev. Lett.* **2010**, *104*, 238104.
- [42] A. Goriely, M. Nizette, M. Tabor, *J. Nonlinear Sci.* **2001**, *11*, 3.
- [43] T. Li, Z. G. Suo, S. P. Lacour, S. Wagner, *J. Mater. Res.* **2005**, *20*, 3274.
- [44] M. Gonzalez, F. Axisa, M. V. Bulcke, D. Brosteaux, B. Vandeveld, J. Vanfleteren, *Microelectron. Reliab.* **2008**, *48*, 825.
- [45] D. H. Kim, N. S. Lu, R. Ma, Y. S. Kim, R. H. Kim, S. D. Wang, J. Wu, S. M. Won, H. Tao, A. Islam, K. J. Yu, T. I. Kim, R. Chowdhury, M. Ying, L. Z. Xu, M. Li, H. J. Chung, H. Keum, M. McCormick, P. Liu, Y. W. Zhang, F. G. Omenetto, Y. G. Huang, T. Coleman, J. A. Rogers, *Science* **2011**, *333*, 838.
- [46] Y. H. Zhang, S. D. Wang, X. T. Li, J. A. Fan, S. Xu, Y. M. Song, K. J. Choi, W. H. Yeo, W. Lee, S. N. Nazaar, B. W. Lu, L. Yin,

- K. C. Hwang, J. A. Rogers, Y. Huang, *Adv. Funct. Mater.* **2014**, *24*, 2028.
- [47] Y. H. Zhang, S. Xu, H. R. Fu, J. Lee, J. Su, K. C. Hwang, J. A. Rogers, Y. Huang, *Soft. Matter* **2013**, *9*, 8062.
- [48] Y. A. Huang, Y. Z. Wang, L. Xiao, H. M. Liu, W. T. Dong, Z. P. Yin, *Lab Chip* **2014**, *14*, 4205.
- [49] T. Widlund, S. X. Yang, Y. Y. Hsu, N. S. Lu, *Int. J. Solids Struct.* **2014**, *51*, 4026.
- [50] S. X. Yang, Y. C. Chen, L. Nicolini, P. Pasupathy, J. Sacks, B. Su, R. Yang, D. Sanchez, Y. F. Chang, P. L. Wang, D. Schnyer, D. Neikirk, N. S. Lu, *Adv. Mater.* **2015**, *27*, 6423.
- [51] S. X. Yang, B. Su, G. Bitar, N. S. Lu, *Int. J. Fracture* **2014**, *190*, 99.
- [52] S. S. Yao, Y. Zhu, *Adv. Mater.* **2015**, *27*, 1480.
- [53] A. E. H. Love, *A Treatise on the Mathematical Theory of Elasticity*, Cambridge University Press, New York, NY, USA **2013**.
-